Journal of Power Sources 591 (2024) 233804

Contents lists available at ScienceDirect

Journal of Power Sources

journal homepage: www.elsevier.com/locate/jpowsour

Towards understanding the functional mechanism and synergistic effects of $LiMn_2O_4$ - $LiNi_{0.5}Mn_{0.3}Co_{0.2}O_2$ blended positive electrodes for Lithium-ion batteries

Dimitrios Chatzogiannakis [a,c,d,1], Marcus Fehse [a,1], Maria Angeles Cabañero [a,b,1], Natalia Romano [a], Ashley Black [c], Damien Saurel [a], M. Rosa Palacin [c,*], Montse Casas-Cabanas [a,e]

[a] Centro de Investigación Cooperativa de Energías Alternativas (CIC energiGUNE), Basque Research and Technology Alliance (BRTA), 01510 Vitoria-Gasteiz, Spain
[b] FEV Iberia SL, C/Gardoqui 1 48008 Bilbao, Spain
[c] Institut de Ciència de Materials de Barcelona, ICMAB-CSIC, Campus UAB, 08193 Bellaterra, Catalonia, Spain
[d] ALISTORE-ERI, CNRS FR, 3104, France
[e] Ikerbasque - Basque Foundation for Science, Maria Diaz de Haro 3, 48013 Bilbao, Spain

HIGHLIGHTS

- LMO-NMC blended electrodes were tested and investigated by operando (XRD and XAS).
- An overall rate capability gain is achieved for specific blend compositions.
- Effective current load on each component differs from the nominal applied rate.
- Operando studies confirm that current load peaks spur the redox reactions.

ARTICLE INFO

Keywords:
Blend electrodes
LMO-NMC
Operando XAS
Operando XRD

ABSTRACT

Blended positive electrodes consisting of mixtures of $LiMn_2O_4$ spinel (LMO) and layered $LiNi_{0.5}Mn_{0.3}Co_{0.2}O_2$ (NMC) have been studied by coupling electrochemical testing to *operando* synchrotron based X-ray absorption and powder diffraction experiments to shed light on their redox mechanism. Blending NMC with LMO results in enhanced energy density at high rates, with the composition with 25% LMO exhibiting the best electrochemical performance. Tests with a special electrochemical setup detecting the contribution of each blend component indicate that the effective current load on each blend component can be significantly different from the nominal rate and also varies as function of SoC. *Operando* studies enabled to monitor the evolution of oxidation state and changes in the crystal structure, which are in agreement with the expected behaviour of the individual components considering the material specific electrochemical current loads. These findings should contribute to a deeper mechanistic understanding of blended electrodes to foster a rational driven approach for their design.

1. Introduction

"Blended" positive electrodes with multiple active materials pose an interesting and industrially relevant approach to overcome intrinsic disadvantages of certain single compounds. Mixing materials in the right proportion can potentially give rise to improvements in a variety of properties. Several works have reported enhanced thermal stability [1,2], increased rate capability [3] and extended cycle life via blending, in particular for $LiMn_2O_4$, which exhibits fast kinetics but limited capacity [2,4,5].

Numerous studies on $LiNi_xMn_yCo_zO_2$ (where x+y+z = 1, often referred to as NMC-XYZ e.g. NMC-111, NMC-532, NMC-811, etc.) have shown that electrochemical performance is significantly dependent on the relative transition metal ratios. A general understanding of the phase diagram of NMCs is that increasing the amount of cobalt favours the lithium (de)intercalation reaction kinetics, high nickel content improves capacity and raising the amount of manganese favours thermal stability (and hence safety) and lowers cost [6]. The current trend in commercial batteries is oriented towards increasing the nickel

* Corresponding author.
E-mail addresses: rosa.palacin@icmab.es (M.R. Palacin), mcasas@cicenergigune.com (M. Casas-Cabanas).
[1] Authors contributed equally.

https://doi.org/10.1016/j.jpowsour.2023.233804
Received 11 August 2023; Received in revised form 6 October 2023; Accepted 29 October 2023
Available online 22 November 2023

share to enhance capacity and reduce cobalt content due to environmental, cost, supply and ethical concerns. Blends of either NMCs or NCA ($LiNi_xCo_yAl_zO_2$ where x+y+z = 1) with olivine-type materials (LiFePO4, $LiFe_xMn_yPO_4$, x+y = 1) or $LiMn_2O_4$ have been studied to combine the high capacity of the former with the lower cost and higher power capability of the latter [7]. For that case, improved shelf and cycle life compared to pure LMO was also achieved thanks to the mitigation of Mn dissolution [8–10]. Blends of LMO and NMC are already being widely used in commercial batteries for EV's in addition to other, less specialized applications [1,5,8,11,12].

Still today, commercial blends are primarily chosen based on empirical evidence, and the mechanistic understanding of the individual contribution of each component and their interplay remains unclear, even after several noteworthy works in the field [13,14]. According to a theoretical multi-particle model, it was proposed that the flow of current across each component in the blend is different, with the material possessing faster kinetics having a higher capacity to accommodate lithium during galvanostatic discharge pulses. This surplus lithium is then redistributed during the subsequent relaxation period, which is commonly referred to as the "buffer effect" [15]. This effect was experimentally evinced by Klein et al. [16] by means of X-ray diffraction for the $LiFe_{0.3}Mn_{0.7}PO_4$ - $LiMn_{1.9}Al_{0.1}O_4$ system. Heubner et al. were able to quantify it by using an electrochemical cell set-up with two working electrodes (each one with one component material of the blend) that allows to determine the current contribution of each material separately [17]. The same group applied this technique to different blend combinations LMO-NMC, LCO-LMO [18], LFP-LCO [7] and LMO-LFP [19], observing that each material is subjected to a different electrochemical load (current) with its effective C-rate often being several times higher (or lower) than the C-rate of the cell. Recently Liebmann et al. demonstrated that the basic electrochemical properties of the blend's components match those of a physical mixture model hence objecting to a systematic change of the thermodynamic and kinetic properties of the mixture [20].

One of the few mechanistic studies on the LMO-NMC system was carried out by Kobayashi et al. using X-ray diffraction to follow the changes in the lattice parameters of the blends at low and high rates for fresh and degraded cathodes. The conclusion was that the reduction of capacity at higher rates (C/2 vs. C/20) was due to limited insertion of Li ions in NMC during discharge [21]. In agreement with previous studies they also observed Li exchange between active materials during relaxation periods between charge and discharge after extensive cycling.

Herein we present a study on the LMO - NMC-532 aiming at elucidating the synergistic effects, examine their correlation with the blend composition and investigate the redox mechanism by combining electrochemical and *operando* synchrotron based spectroscopic and diffraction techniques. Through the comparison and contrasting of those insights we strive to contribute to a better understanding of the working principle of such blends and advance towards a more rational approach in their design.

2. Experimental details

2.1. Electrode formulation and cell assembly

The materials used were all of commercial grade. $LiMn_2O_4$ (LMO) and $LiNi_{0.5}Mn_{0.3}Co_{0.2}O_2$ (NMC-532) were purchased from Sigma-Aldrich and MTI corp., respectively. The microstructure of the two materials was quite different with $LiNi_{0.5}Mn_{0.3}Co_{0.2}O_2$ secondary particles in micrometer size (D_{50} = 10.0 – 14.0 μm) composed of primary aggregated particles with diameters around 300–500 nm and $LiMn_2O_4$ particles exhibiting diameters smaller than 500 nm (data provided by supplier and verified by SEM and TEM, see Fig. 1(a) and (b) in S.I., respectively).

Slurries of the pure materials and three different LMO:NMC-532 blends were prepared, namely L25:N75, L50:N50 and L75:N25 based on their weight percentage, by dispersing the mixture of active materials in N-Methyl-2-pyrrolidone, NMP, along with Polyvinylidene fluoride, PVDF binder (Solef 5130/1001, Solvay, Belgium), and carbon additive (C65, Imerys, Switzerland) in a ratio of 84:8:8. Subsequently, and after homogenizing through vigorous stirring (ULTRA-TURRAX T25, IKA Germany) the slurries were tape casted on 18 μm Al foil as current collector. The capacity loading was generally adjusted to 1 ± 0.25 mAh cm^{-2}, except for the case of the power performance tests (Fig. 1) where it was kept to 1 ± 0.05 mAh cm^{-2} for the sake of a rigorous comparison. For the calculation of the areal capacity loadings, the expected cell capacities and the C-rate calculation, the capacity of the materials measured as C/20 in the same electrochemical window was used (167 mAh/g for NMC-532 and 121 mAh/g for the LMO).

A cross sectional micrograph of a 50:50 blend electrode is depicted in Fig. 1(c) in the S.I. In the micrograph, easily distinguishable are the micrometer sized NMC-532 particles which are homogeneously surrounded by the LMO sub-micron sized ones as evinced by elemental mapping see Fig. 1(d). Blend electrodes are compact and crack-free, which validates the quality of the tape casting process.

Electrodes consisted of discs of 14 mm diameter cut from the above mentioned tapes, which were pressed at 4 tons using a hydraulic press and subsequently dried at 120 °C under vacuum for at least one hour. Afterwards and without any exposure to air they were used as working electrodes for cell assembly in an argon-filled glove-box (≤ 0.1 ppm H_2O and O_2) using a quartz fibre separator (QM-A; Whatman, 475 μm) and a 16 mm diameter lithium disc as counter-electrode. From the mass of the Lithium (≈50 mg) the capacity of the electrode was found to be 192 mAh vastly larger than the typical working electrode capacity of less than 2 mAh. The thickness of the working electrodes was found to be 60–70 μm before calendering, reducing to ≈ 50 μm after, yielding a density of ≈ 1.5 gcm^{-3}. Approximately 300 μL of a commercial 1:1 EC/DMC mixture with 1M $LiPF_6$ and 2% VC was used as electrolyte (Solvionic, France). Electrochemical performance was tested using CR2032 coin cells and cycled using a VMP-3 potentiostat-galvanostat (Bio-Logic, France) within the voltage window of 3.2 to 4.3 V vs. Li^+/Li and at room temperature. All the post-formation reported cycles had coulombic efficiencies higher than 95%.

The electrochemical cycling during *operando* measurements were carried out using a VSP potentiostat-galvanostat (Bio-Logic, France) at C/4 rate in CC mode within voltage window of 3.2 to 4.3 V vs. Li^+/Li.

For the *operando* experiments, identical electrodes as for the electrochemical experiments were used with active material loading of around 7 mg cm^{-2} in a specially designed *in situ* cell for *operando* spectroscopic measurements, recently described elsewhere [22]. For the diffraction experiment CR2032 coin cells equipped with glass window were used.

2.2. Decoupled blended electrode setup

In order to further investigate the electrochemical stress (current load) experienced by each material in the blends, a cell setup with decoupled blend component electrodes was used with electrodes and separators identical to the previously mentioned. The assembly was done as previously described by Heubner et al., in a three electrode PFA swagelok type cell with two electrodes containing one of the blend components each, with an appropriate active mass ratio to mimic the mixed blend (tuned by electrode diameter). The two electrodes, along with two separator discs, were placed facing each other while having a piece of perforated, properly shaped, lithium in between, as counter electrode. The same, previously discussed electrolyte was used but approximately double the amount of a coin cell (≈ 600 μL). For the measurement, two channels of a potentiostat/galvanostat (BioLogic VMP-3) were used. One of them supplied the cycling current to one of the positive electrodes, while the other held the two positive electrodes at the same potential (ΔV = 0 V) recording the current of the second electrode.

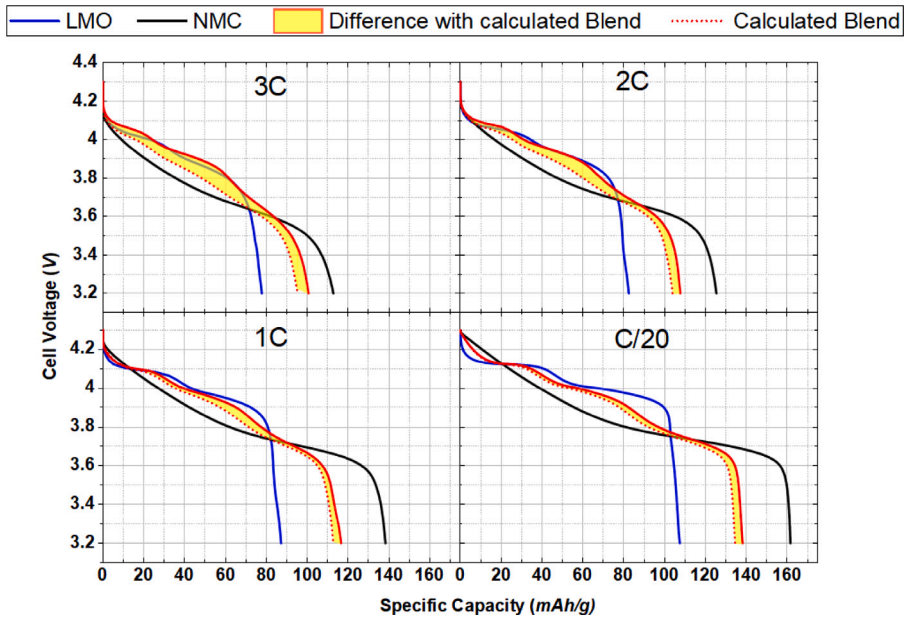

Fig. 1. Cell voltage vs specific capacity curves during discharge at different cycling rates for a L50:N50 blend (solid red line), pure LMO (blue), pure NMC-532 (black) as well as calculated blend (dotted red line). The difference between the calculated and experimentally observed electrochemical cycling curve reflecting the synergistic effect is highlighted in yellow. (For interpretation of the references to colour in this figure legend, the reader is referred to the web version of this article.)

2.3. Operando X-ray diffraction

XRD measurements were carried out on MSPD beamline at the ALBA synchrotron using 15 keV photon energy (λ = 0.82572 Å) in transmission geometry using a MYTHEN high-throughput position sensitive detector for the 2Θ range 1.5 to 61°. The cells used were specially adapted CR2032 coin cells (Institute for Applied Materials - Energy Storage Systems Karlsruhe Institute of Technology), bearing a thin glass window on both sides and a hole on the stainless steel spacer but otherwise identical to the standard ones. A VSP potentiostat-galvanostat (Bio-Logic, France) was utilized in CC/CV (1h CV + 1h OCV) mode and cells were cycled at C/4. The cells were mounted on an 8 coin cell carousel-like holder enabling sequential data acquisition [23] with an interval of 5.5 min between patterns for each cell. Structural analysis was performed by means of Rietveld refinements using the FullProf software [24]. The peaks from the Aluminium current collector were included in Le Bail mode.

2.4. Operando dual edge X-ray absorption spectroscopy

XAS measurements at the Ni and Mn K-edge were carried out in transmission mode at the CLAESS beamline at ALBA synchrotron. A specially designed *in situ* cell, recently described elsewhere [22], was placed between the first and second ionization chambers. A focusing double-crystal Silicon (311) monochromator was used and beam size was adjusted to 3 × 1 mm (V×H). XAS spectra were continuously acquired during one complete electrochemical cycle, alternating every 10 min between the two transmission metal edges (Ni and Mn). For energy calibration, transition metal (TM) reference foils placed between the second and third ionization chambers were used. Cycling protocol and equipment was identical to the one used in the XRD measurement, excluding the OCV step.

2.5. Chemometric data analysis

The complete *operando* XAS datasets were analysed by combining Principal Component Analysis (PCA) and Multivariate Curve Resolution-Alternating Least Squares (MCR-ALS) analysis, see details elsewhere [25]. The MCR-ALS analysis for XAS data set was carried out with the following constraints: non-negativity of the concentration of the components and closure (sum of the components concentrations equal to 100%) as well as single component at beginning of discharge. For Mn a less or equal to 1 closure constrain had to be used to achieve a converging fit.

3. Results

3.1. Electrochemical performance of blends

The electrochemical performance of the three different LMO:NMC blended positive electrode materials (25:75, 50:50 and 75:25 wt%) was tested against lithium metal at coin cell level and compared with that of electrodes made with only one of the components. Fig. 1 shows the measured and calculated voltage vs. capacity profiles upon discharge at different C-rates of the individual components (LMO, NMC-532) and the 50:50 wt% blend. The calculated profile capacity was achieved from the weighted average of the capacity of the two individual materials using their mass fraction as the weighting factor, as was previously reported by Jung et al. [26] (equation in S.I.). No significant differences between the expected and the experimentally obtained curves are observed at low cycling rate (C/20). However, as cycling rate is increased to 1C, 2C and 3C, a growing mismatch between them can be appreciated, which is highlighted by the yellow area in Fig. 1 . A higher average discharge voltage is observed experimentally, the magnitude of which grows with cycling rate (1, 3 and 5 mV respectively). This results in an enhanced specific capacity (vs the calculated) for 1 C, 2C and 3C of 3.5, 3.8 and 5.8 m Ah g^{-1}, respectively. A similar trend was observed for the L25:N75 blend depicted in Fig. 3, in the S.I.. These observations are the manifestation of the previously suggested synergistic effect achieved in the blends when compared to sum of the individual components [1,11,12] .

In order to investigate the impact of blending ratio, a study on the C-rate performance and capacity retention was performed where the different blends where first subjected to multiple cycling rates (from C/20 up to 3C) followed by 100 cycles at 1C. At least four cells were used for each measurement with their loading adjusted at 1 ± 0.25 mAh cm^{-2} for reproducibility. Thanks to the higher discharge voltage of LMO compared to NMC-532, we witness a gradual increase of the

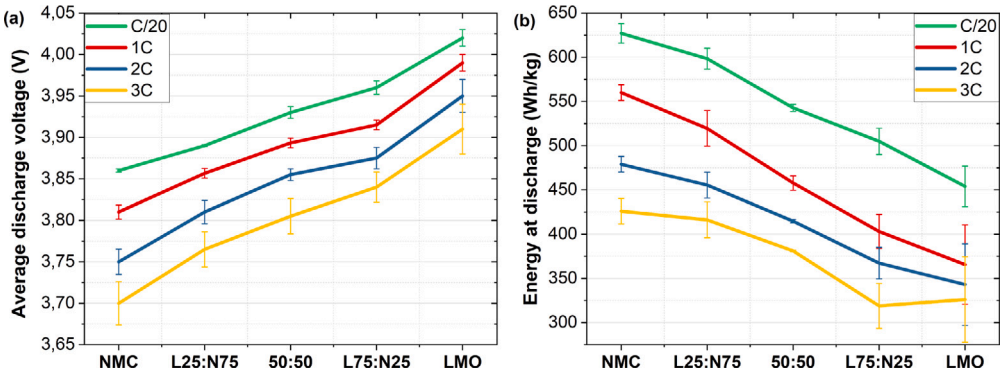

Fig. 2. Comparison between single-component electrodes and L25:N75, L50:N50 and L75:N25 blends for (a) discharge voltage and (b) discharge energy at C/20, 1C, 2C and 3C. All results are averaged based on four cells, with bars depicting standard deviations.

blend's average voltage with increasing LMO content (see Fig. 2(a)). The spread of the curves gives information about the overpotential growth with faster rates and even though pure LMO is less affected by rate than pure NMC, the results are inconclusive for the blends. In spite of the voltage benefit stemming from LMO addition, the increase in its content also results in a decrease in energy density due to its significantly lower specific capacity, see Fig. 2(b). Interestingly, the L25:N75 blend provides comparable energy density to the pure NMC-532, particularly at higher rates. This blend ratio is hence of particular interest and was selected for mechanistic investigation, *vide infra*. It should be noted that this 25% LMO addition results not only in cost reduction but also in a more sloping electrochemical signature which could facilitate SoC estimation compared to pure NMC. Furthermore, our blend comparison results also show that by adding just 25% of NMC-532 to LMO, the cyclability of LMO, which is prone to fading, can be greatly improved up to the level of pure NMC-532, see Fig. 2 (S.I.). Such a stabilization of LMO by blending has been previously reported [5,8].

3.2. Decoupled blends

For the decoupled blended electrode study, the L25:N75 and L75:N25 blends were selected and each cell was subjected to subsequent charge and discharge cycles. Fig. 3 summarizes the data corresponding to a C/5 (0.2 C) discharge, a rate comparable to the one used for the *operando* studies. The current recorded for each material in the blend was divided by its theoretical capacity to obtain the effective C-rate, indicative of the real current load each electrode material is bearing.

As expected, due to their very different characteristic electrochemical curves and power capabilities, the effective C-rate of the two materials varies constantly depending on the state of charge (SoC) of the blend. The influence of the LMO voltage plateaus is highlighted by the fact that its discharge C-rate increases drastically when the voltage of the cell coincides with them, resulting in two characteristic peaks in the effective C-rate plot. However, their maximum effective C-rate value depends strongly on the fraction of LMO in the blend. For the L25:N75, the effective rate on LMO reaches up to 0.65 C, more than three times the applied C rate and twice as high as the maximum current load for L75:N25, which peaks at 0.3 C. Also, since LMO in L25:N75 practically contributes during 40% of the overall discharge time (10%–50% of overall progress of discharge) it discharges 2.5 times faster than expected by the cell's C-rate (in 120 min instead of 300 for C/5 rate). On the other hand, NMC-532 takes most of the current load at lower SoC due to its lower average potential, the value being again highly dependent on its weight fraction in the blend. For the blend with minority share of NMC (L75:N25), it reaches three times the total applied rate of the cell. This highlights that the effective C-rate of the blend constituents can differ significantly from the nominal cell C-rate and is an important factor that should be taken into account for rational

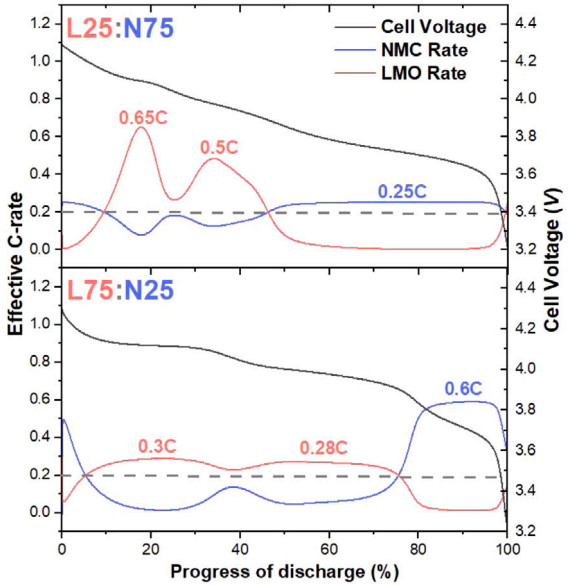

Fig. 3. Decoupled blended electrode tests for L25:N75 (Top) and L75:N25 (Bottom) at C/5 (0.2C). The red (LMO) and blue (NMC-532) lines depict the effective C-rate of each electrode component, with explicit values corresponding to maximum observed C-rate. C-rates are calculated from the current flowing through each electrode component, which is divided by its capacity. The grey dashed line is the overall nominal cell current divided by the sum of the capacities of both positive electrodes (set at C/5). (For interpretation of the references to colour in this figure legend, the reader is referred to the web version of this article.)

design of blended electrodes. To further understand the behaviour of each component, the decoupled blends study for the L25:N75 blend was extended to higher rates (up to 3C) and the results are shown comparatively in Fig. 4. Immediately apparent is that the deviation of each component's effective C-rate from the cell nominal C-rate differs significantly, easily noticable at higher rates, especially for the minority component (in this case LMO). At 3C the effective C-rate of LMO ranges from 0.4C to 5.2C while that of NMC is comprised between 2.4C to 3.7C. These data highlight that the ratio of the active components becomes even more relevant at high C-rates. Noteworthy is also the fact that LMO maintains its characteristic double peak behaviour for all the tested rates, although experiences C-rate dependent alterations. Going to higher discharge rates causes the shift of the peaks to higher specific capacities and broadens them. Insights on the synergetic phenomena arise when one calculates the ratio between effective and nominal C-rate. At 0.1C (C/10) nominal cell rate, the maximum effective C-rate experienced by LMO was found to be 0.3C, three times that of the nominal. This differs significantly from the discharge at a 3C nominal

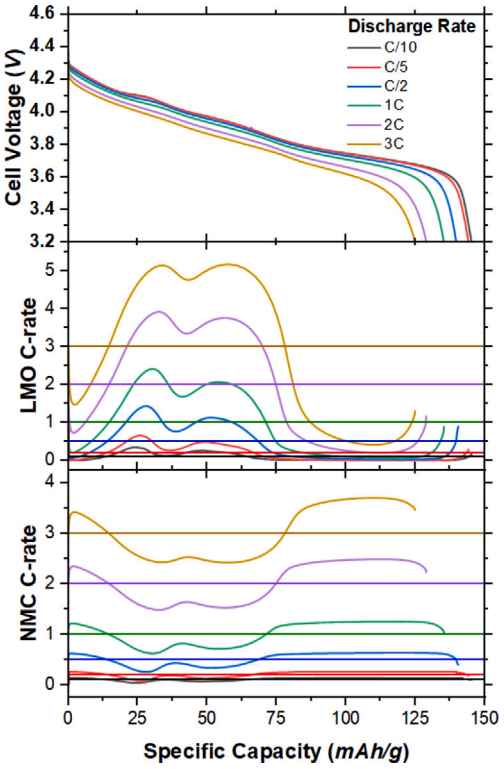

Fig. 4. Decoupled Blend L25:N75 tested at multiple rates. The characteristic curves of the blend are depicted for each rate (top) and below are shown the effective C-rates that were determined for each component, LMO (Middle) and NMC-532 (Bottom). Horizontal lines indicate the cell's nominal C-rate.

cell rate where LMO experiences a maximum slightly above 5C, only 1.7 times higher. Thus, at high rates within the range of 10–90 mAh/g where LMO is active, the two components function more cooperatively altering the load share, which leads to the performance increase observed in Fig. 1. Based on the aforementioned analysis one can conclude that on Fig. 1, the rule of mixture calculation fails to describe the properties of the blend because it assumes equal current load on both electrode components. This is not the case as LMO takes the majority of the current at high voltages (high SoC). The overpotential of the blend should be dictated mainly from the voltage of the primarily active component at the effective C-rate. Interestingly, even though blended LMO discharges at an effective C-rate significantly larger than the cell's nominal, its overpotential is comparable to the one observed for pure LMO at 3C. The resulting increase in the average discharge voltage of the blended cathode allows the retrieval of higher specific capacity values before the cell reaches its lower cut-off voltage, as seen in Fig. 1.

3.3. Operando XRD and XAS

Based on its better electrochemical cycling performance (*vide supra*), the L25:N75 blend was selected for an in depth *operando* study acquiring either X-ray diffraction patterns or X-ray absorption near edge spectra (XANES) while being subjected to lithiation (discharge) or delithiation (charge) current at C/4. While XRD provides information on long-range structural changes such as phase transitions and variations in lattice cell parameters, the XANES spectra presents insights into oxidation state and local coordination geometry changes of the probed transition metal.

The diffraction patterns in selected angular ranges for a full cycle (discharge + charge) along with the corresponding electrochemical curve are shown in Fig . 5.

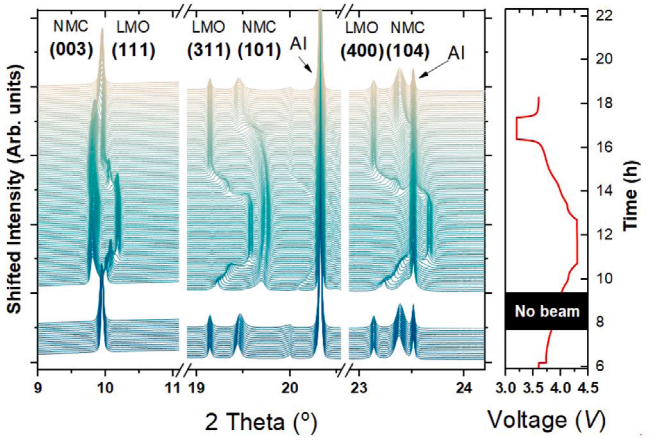

Fig. 5. Evolution of diffraction patterns of a L25:N75 blend electrode *operando* upon discharge and charge at C/4. *hkl* Miller indices are given for selected peaks corresponding to NMC and LMO phase. Peaks corresponding to Al current collector are also indicated. Blank area marks a period of beam loss.

Gradual changes in terms of peak position and intensity are observed during charge and discharge from which the evolution of lattice parameters (and hence cell volume) and phase changes can be deduced by means of multi-phase Rietveld refinement. A single phase with $R\bar{3}m$ space group was selected to represent NMC-532 throughout the full cycle while three phases with the same, $Fd\bar{3}m$ space group were considered for LMO because it undergoes through two phase transitions.

The refinement of the diffraction patterns reveals that the cell volume of both materials decreases during charge (delithiation), expressed by a general shift of diffraction peaks to higher angles. An exception to this is the (003) peak of the NMC-532 phase, as an increase in interlayer distance is observed, in agreement with the literature [27]. This specificity of NMC-532 (and all layered oxides in general) is commonly explained by the increasing electrostatic repulsion between the positively charged MO_6 slabs. It has been reported that the interlayer distance reduces abruptly at high delithiation degree caused by the decrease of the repulsion between O^{-2} layers as the metal-oxygen bonds become more covalent [28,29]. In our *operando* diffraction data we only see the onset of this effect at the upper cut-off voltage at 4.3 V. Regardless of this *c* cell parameter increase, while *a* and *b* decrease, as evidenced by the (101) and (104) peaks shift towards higher angles, an overall monotonically cell volume contraction upon charge occurs.

While a continuous shift in the peak positions is observed for NMC-532, in agreement with a single phase reaction mechanism involving the formation of a solid-solution, a different evolution is observed for the LMO (111) peak, in agreement with its well known redox mechanism involving two successive phase transitions during charge (i.e. different LMO phases, differing in Li content, co-exist for the same SoC). To monitor changes as a function of SoC, the global LMO cell volume was calculated as the weighted average of the cell volumes of the co-existing LMO phases and is depicted as solid red lines without markers in Fig. 7 together with that of NMC-532 (bottom and top respectively). The evolution of phase weight fractions is depicted in Fig. 4 in S.I. The trends observed upon charge are fully reversed during the discharge (lithiation) in agreement with the high reversibility of the structural changes of NMC-532 and LMO.

To obtain complementary information on the local structure and electrochemical activity of the redox active transition metal (TM) the L25:N75 blend was also investigated by dual edge *operando* XAS under similar experimental conditions, however starting with pre-charged cells.

The evolution of both Mn and Ni XANES K-edges upon delithiation and lithiation are depicted in Fig. 6 along with the corresponding

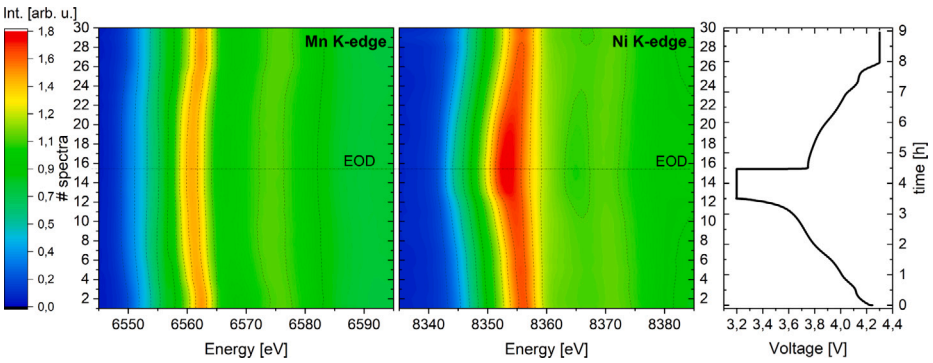

Fig. 6. Evolution of Mn (left) and Ni (right) K-edge XANES spectra upon discharge and charge under *operando* conditions.

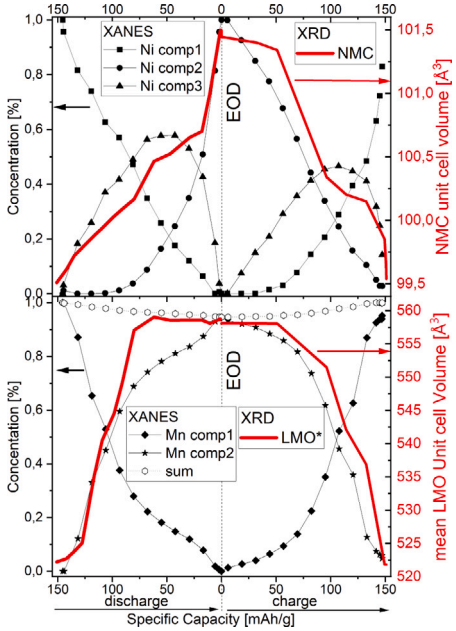

Fig. 7. Concentration profiles based on XANES analysis (black line with markers) for Ni (top) and Mn (bottom) and unit cell volume evolution (solid red lines without markers) based on *operando* XRD for NMC-532 (top) and LMO (bottom) as function of specific capacity. The dashed line with hollow markers in bottom figure represents the sum of the two XANES-derived Mn components. The mean LMO unit cell volume was calculated by multiplying the lattice volume of individual LMO phases with their corresponding phase fraction. The vertical dashed line indicates the end of discharge (EOD). (For interpretation of the references to colour in this figure legend, the reader is referred to the web version of this article.)

electrochemical curve. It should be noted that XAS spectra represent the sum of all absorbers within the beam path, hence, for a LMO:NMC blend, the Mn K-edge will comprise both the LMO and NMC-532 contribution, while for Ni K-edge NMC-532 is the only contributing species. A gradual shift to lower energies is observed upon discharge (lithiation) for both TM edges which reflects the lowering of the mean oxidation state of the TM. Interestingly the main spectral changes of the two TM do not coincide. While for the Mn edge (Fig. 6, left) the main changes are observed during the first few spectra (≤#6), the changes on the Ni edge are strongest towards the end of the discharge (#8 to 14). This underlines the usefulness of element specific XANES analysis as in the electrochemical curve no distinct plateaus can be identified and the slope changes are barely visible. Upon charge (delithiation, >#16) the observed changes are largely reversed, which suggests a good reversibility of the TM redox reaction.

These spectral data sets were further analysed using a statistical tool based on PCA followed by MCR-ALS, see Fig. 6 in S.I. The results obtained suggest that the full spectral data set of Ni K-edge can be reproduced with a linear combination of three components. This is well in line with the expected reduction of Ni^{+4} to Ni^{+2} via the intermediate Ni^{+3} phase upon NMC-532 discharge, see Fig. 7(top). For Mn K-edge the spectral changes can be reproduced analogously using two components which is in agreement with the expected reduction of Mn^{+4} to $Mn^{+3.5}$ during LMO lithiation. It should be noted that the statistical approach used for the concentration profile plotting only takes into consideration the spectral changes in the data set. Absorbing atoms that do not change their coordination geometry and /or chemical state leading to spectral alterations are hence not considered. Interestingly, the closure condition (sum of components equal to one) could not be achieved for the Mn spectral data set unlike for Ni. This indicates that there are additional spectral changes which are not considered by the evolution of the two components. It is likely that these additional unaccounted for spectral changes originate from the Mn in the NMC-532, which represents ≈46% of the total Mn present in the blend electrode. Although the Mn in NMC-532 is not expected to undergo any change in the oxidation state, it experiences alterations in its ligand field caused by the reduction and oxidation of the redox active Ni in its vicinity which result in alterations of the Mn K-edge XANES spectra [30,31], as we have recently evidenced for another high voltage positive electrode material [32]. This hypothesis is also supported by the fact that the largest mismatch between closure condition equal to one and the sum of the two Mn components is found between spectra #10 to 20, which is the region where the strongest Ni spectral changes occur, see dotted line with hollow markers in Fig. 7 (bottom). The pure Ni and Mn XANES spectral components associated to the concentration profiles depicted in Fig. 7 are shown in Fig. 7 of the S.I. along with metal oxide reference spectra to fingerprint their approximate oxidation state. The results depicted in this figure strengthen the assumption that the three Ni components can be roughly ascribed to the Ni^{+2}, Ni^{+3} and Ni^{+4} in NMC-532. In fact a good agreement between Ni comp2 and Ni^{+2} reference is found, underlining that at EOD (End of Discharge) the most reduced state of Ni is prevalent which is closest to the Ni^{+2} state. The deviation from the Ni^{+2} is a consequence of the presence of Ni^{+3}. As Mn and Co have oxidation states equal to +4 and +3 respectively and the average oxidation state of the TMs in NMC is +3, the Ni^{+2}/Ni^{+3} ratio changes depending on the Ni and Mn contents. Thus, Ni^{+3} will be present in pristine NMC's with a content of Ni higher than that of Mn [6,30]. Furthermore, a good agreement is found for Ni comp3 and the Ni^{+3} reference, which accentuates that the formation of a transient phase with an approximate oxidation state of Ni^{+3} occurs. The fingerprint comparison also reveals that, at EOC, at which Ni comp1 is prevalent, the Ni^{+4} state is not reached which suggests an incomplete delithiation. Such incomplete delithiation is to be expected in regard of conservative cycling conditions used here to avoid detrimental structural rearrangement of the NMC phase at high SoC, and has been reported in previous *operando* XAS experiments [30].

Absorption edge position of both pure spectral components of Mn are between the Mn-oxide references of $Mn^{+3.5}$ and Mn^{+4}. Component

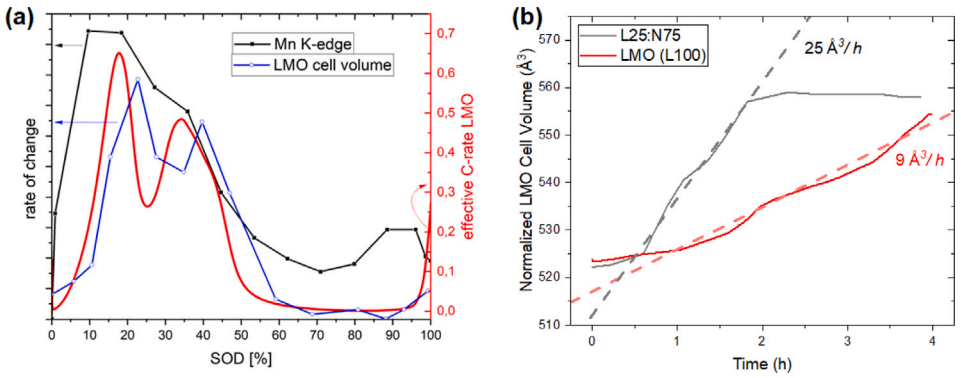

Fig. 8. (a) Rate of change of Mn oxidation state (black line with square markers) and LMO normalized unit cell volume (blue line with hollow spherical markers) along with effective current load rate on LMO (solid red line) as function of state of discharge (SOD) for a L25:N75 blend electrode. (b) LMO normalized unit cell volume as a function of discharge time (at C/4) for the cell with the blended L25:N75 electrode (grey line) and one with pure LMO electrode (red line). The most active regions were linearly fit (dashed lines) and their slope is reported. (For interpretation of the references to colour in this figure legend, the reader is referred to the web version of this article.)

2 is prevalent at EOD and has the oxidation state closest to $Mn^{+3.5}$ reference. This is in agreement with the fact that the mean oxidation state of Mn includes roughly a mix of 55 to 45% of $Mn^{+3.5}$ in LMO and Mn^{+4} of the NMC. Upon delithiation component 1 is formed at higher energies compared to component 2, indicating a higher oxidation state, in agreement with the oxidation of the LMO. Interestingly, the edge position of component 1 is slightly lower than the Mn^{+4} reference, which could originate from an incomplete delithiation of the LMO upon charge reaction at the applied cut-off voltage of 4.3 V.

The findings of *operando* XRD and XANES analyses are summarized in Fig. 7 which depict the correlation between oxidation state and unit cell volume for Ni phase (top) and Mn phase (bottom), respectively. It is remarkable that even though these data come from two independent experiments the gradual growth of the NMC-532 unit cell volume upon lithiation (discharge) is fully congruent with the rise of intermediate nickel component 3, which reflects the reduction of Ni^{+4} to Ni^{+3}, see Fig. 7(top). Upon further lithiation beyond 50 mAh/g an accelerated increase in the NMC-532 lattice volume is observed which coincides with the steep rise of nickel component 2, reflecting the formation of completely reduced Ni^{+2}. Upon subsequent charge (delithiation) up to 100 mAh/g capacity an equally good overlap between the sharp decrease in NMC unit cell volume and the decline of component 2 is observed. Lithiation beyond this capacity results in a less steep shrinkage of lattice volume, which analogous to the discharge reaction, coincides with the formation of the intermediate Ni^{+3} (component 3). Towards the end of charge a steep decline of both cell volume and concentration of intermediate component 2 are observed. Interestingly, an asymmetry between discharge and charge is observed both for the Rietveld refinement derived volume change and the XAS derived concentration profiles, which could be due to overpotential build-up. Such a good agreement between two separate *operando* experiments is remarkable and underlines the reproducibility of the experimental findings.

The Mn XAS and XRD LMO data illustrate that the main unit cell volume change and oxidation state changes occur in the capacity range of 150 to 100 mAh/g during discharge, and 100 to 150 mAh/g during charge. Within this range, the rapid decay of Mn component 1 and the rise of component 2 occurs, reflecting the reduction from Mn^{+4} to $Mn^{+3.5}$ and a rapid increase in mean unit cell volume of the LMO phases. In the capacity range from 100 mAh/g discharge to 100 mAh/g charge a single LMO crystal phase is prevalent (see Fig. 4 S.I. for individual phase volumes and fractions), for which only minor volume changes are observed. This is well in line with the broad maximum of the spectroscopic species Mn component 2, reflecting the redox inactivity of the Mn TM in this region.

In summary, our combined XAS and XRD analysis shows that during charge (delithiation) of a L25:N75 blend the subsequent oxidation of firstly Ni and secondly Mn occurs which is accompanied by a contraction of the cell volume for both components (NMC-532, LMO). This sequence is reversed upon discharge.

To visualize the correlation between the redox mechanism progression and the fluctuating effective current load in the L25:N75 blend electrode, the rate of change of oxidation state of Mn (based on XANES) and of the LMO unit cell volume (based on XRD) are superimposed with those of effective C-rate on LMO in Fig. 8(a). A general agreement between the effective C-rate on the LMO and the oxidation state changes of the Mn K-edge is found depicting a twin peak, despite a much lower resolution of the latter and slightly higher applied C-rate (C/4 instead of C/5). In fact the maxima at ≈15 and 35% of SOD of the effective current rate on LMO phase are well aligned with the maxima and shoulder peak position of the Mn K-edge change rates. This confirms that when LMO phase bears highest current rate it undergoes the fastest redox reaction. To further support this claim, the normalized unit cell volume of a pure LMO electrode (see Fig. 5 in S.I.) as determined from *operando* XRD refinements at C/4 are plotted as a function of discharge time alongside those of the L25:N75 blend Fig. 8(b). There is an apparent difference in the behaviour of the normalized unit cell volume of LMO in pure compared to blended electrode. Even though the start and end points are similar, blended LMO is active only during the first 2 h (or approx. 50% SOD) as also observed in the decoupled blend study. In an effort to quantify the difference in the reaction rate, the most active regions of each curve were linearly fit in order to calculate an average rate of change (expressed as Å/h) of LMO normalized unit cell volume. An ≈ 2,8-fold increase in reaction rate was observed when the material is in the L25:N75 blend (25 Å/h compared to 9 Å/h), very close to the 2.5-fold increase observed in the decoupled blend study (*vide supra*).

It should be noted that the sharp twin peak behaviour of the effective rate across the LMO phase depicted in Fig. 8(a) is specific to the L25:N75 blend ratio. Increasing the LMO content in the blend is expected to lower the peak maxima and increase the width of the peaks, as observed for the L75:N25 blend (*vide supra*). In the extreme case of a pure LMO electrode a constant rate is to be expected, equal to the cell's rate. Interestingly, a similar trend of twin peaks is also observed for the change rate of the Rietveld-refined LMO unit cell volume. However, in this case, the peaks are slightly shifted to higher SOD which suggests that the phase transformation reaction is somewhat delayed with respect to the effective current load and oxidation state changes. This delay between XAS and XRD has been previously attributed to domain growth [33]. Nevertheless the general agreement between the three independent experiments (decoupled electrode, *operando* XAS and *operando* XRD) underlines the reliability of our findings.

4. Conclusions

Our results confirm that blending NMC with LMO is a viable approach to unlock synergistic effects in terms of energy density, rate capability and cycling stability. We find that the effective current load on each blend component greatly differs both as function of SoC as well as of its share in the mixture. In this regard, we have demonstrated that the minority component is subjected to a much higher effective current load resulting in higher electrochemical stress. It is hence crucial for rational blend design to select a minority component with fast reaction kinetics in order to yield to a net performance gain. We highlight that these effective current load peaks spur the redox and phase change reaction. Furthermore the *operando* diffraction and spectroscopic analysis confirms that the reaction mechanism occurs via phase transition involving the $Mn^{+3/+4}$ redox couple in the LMO and via solid solution mechanism involving $N^{+2/+4}$ redox couple with a transient Ni^{+3} in the NMC. Moreover, we underline the correlation between lattice contraction and expansion upon oxidation and reduction of the redox active TM. The dual edge XAS unveils that the $Mn^{+3/+4}$ reaction in LMO overlaps with the $Ni^{+3/+4}$ reaction in NMC, while the $Ni^{+2/+3}$ redox reaction occurs at a lower voltage range. Overall these findings enhance the understanding of the mechanisms involved and encourage a more methodical approach to designing blend electrodes and emphasize the need for additional research across a broader range of compositions to strengthen insights and inform the design process effectively.

CRediT authorship contribution statement

Dimitrios Chatzogiannakis: Methodology, Investigation, Data curation, Validation, Formal analysis, Visualization, Writing – original draft, Writing – review & editing. **Marcus Fehse:** Methodology, Investigation, Data curation, Validation, Formal analysis, Visualization, Writing – original draft, Writing – review & editing. **Maria Angeles Cabañero:** Methodology, Investigation, Data curation, Validation, Formal analysis, Visualization, Writing – original draft, Writing – review & editing. **Natalia Romano:** Investigation, Data curation, Validation, Formal analysis. **Ashley Black:** Investigation, Writing – review & editing. **Damien Saurel:** Investigation, Writing – review & editing. **M. Rosa Palacin:** Conceptualization, Methodology, Supervision, Project administration, Funding acquisition, Writing – original draft, Writing – review & editing. **Montse Casas-Cabanas:** Conceptualization, Methodology, Supervision, Project administration, Funding acquisition, Writing – original draft, Writing – review & editing.

Declaration of competing interest

The authors declare that they have no known competing financial interests or personal relationships that could have appeared to influence the work reported in this paper.

Data availability

Data will be made available on request.

Acknowledgements

Operando experiments were performed at MSPD & CLAESS beamlines (proposal 2021035098 and 2021095303) at ALBA Synchrotron with the collaboration of ALBA staff. Authors are grateful to ALISTORE ERI and to H. Ehrenberg and his team at KIT for providing access to the 8 coin cell carousel holder. ICMAB-CSIC members thank the Spanish Agencia Estatal de Investigación Severo Ochoa Programme for Centres of Excellence in R&D, Spain (CEX2019-000917-S) and funding through grant PID2020-113805GB-I00. This work has been done in the framework of the doctorate in Materials Science of the Universitat Autònoma de Barcelona and D.C. wants to acknowledge DESTINY MSCA PhD Programme. Authors acknowledge support of the publication fee by the CSIC Open Access Publication Support Initiative through its Unit of Information Resources for Research (URICI). This project has received funding from the European Union's Horizon 2020 research and innovation programme under Grant Agreement No 945357.

Appendix A. Supplementary data

Supplementary material related to this article can be found online at https://doi.org/10.1016/j.jpowsour.2023.233804.

References

[1] J. Wang, Y. Yu, B. Li, P. Zhang, J. Huang, F. Wang, S. Zhao, C. Gan, J. Zhao, ACS Appl. Mater. Interfaces 8 (31) (2016) 20147–20156, http://dx.doi.org/10.1021/acsami.6b06976.

[2] H.Y. Tran, C. Täubert, M. Fleischhammer, P. Axmann, L. Küppers, M. Wohlfahrt-Mehrens, J. Electrochem. Soc. 158 (5) (2011) A556, http://dx.doi.org/10.1149/1.3560582.

[3] H. Kookjin, I. Jehong, L. Jeong-Seon, J. Jeonggeon, K. Seokhun, K. Jaekook, L. Jinsub, J. Electrochem. Sci. Technol. 11 (3) (2020) 282–290, http://dx.doi.org/10.33961/jecst.2019.00661, URL: http://www.jecst.org/journal/view.php?number=334, arXiv:http://www.jecst.org/journal/view.php?number=334.

[4] A. Klein, P. Axmann, M. Wohlfahrt-Mehrens, J. Power Sources 309 (2016) 169–177, http://dx.doi.org/10.1016/j.jpowsour.2016.01.093.

[5] A.J. Smith, S.R. Smith, T. Byrne, J.C. Burns, J.R. Dahn, J. Electrochem. Soc. 159 (10) (2012) A1696–A1701, http://dx.doi.org/10.1149/2.056210jes.

[6] M. Dixit, B. Markovsky, F. Schipper, D. Aurbach, D.T. Major, J. Phys. Chem. C (2017-10-06) http://dx.doi.org/10.1021/acs.jpcc.7b06122, URL: https://pubs.acs.org/doi/pdf/10.1021/acs.jpcc.7b06122, Archive Location: world Publisher: American Chemical Society.

[7] C. Heubner, T. Liebmann, C. Lämmel, M. Schneider, A. Michaelis, ChemElectroChem 5 (3) (2018) 425–428, http://dx.doi.org/10.1002/celc.201700997.

[8] H. Kitao, T. Fujihara, K. Takeda, N. Nakanishi, T. Nohma, Electrochem. Solid-State Lett. 8 (2) (2004) A87, http://dx.doi.org/10.1149/1.1843792.

[9] H.Y. Tran, C. Täubert, M. Wohlfahrt-Mehrens, Prog. Solid State Chem. 42 (4) (2014) 118–127, http://dx.doi.org/10.1016/j.progsolidstchem.2014.04.006, URL: https://www.sciencedirect.com/science/article/pii/S0079678614000156, Functional materials and analytics for high performance lithium ion batteries.

[10] T. Numata, C. Amemiya, T. Kumeuchi, M. Shirakata, M. Yonezawa, J. Power Sources 97–98 (2001) 358–360, http://dx.doi.org/10.1016/S0378-7753(01)00753-4, URL: https://www.sciencedirect.com/science/article/pii/S0378775301007534, Proceedings of the 10th International Meeting on Lithium Batteries.

[11] S.K. Jeong, J.S. Shin, K.S. Nahm, T. Prem Kumar, A.M. Stephan, Mater. Chem. Phys. 111 (2) (2008) 213–217, http://dx.doi.org/10.1016/j.matchemphys.2008.03.032, URL: https://www.sciencedirect.com/science/article/pii/S0254058408001417.

[12] D. Wu, H. Ren, Y. Guo, X. Zhang, Z. Zhang, J. Li, Ionics 25 (4) (2019) 1595–1605, http://dx.doi.org/10.1007/s11581-018-2650-z.

[13] S.B. Chikkannanavar, D.M. Bernardi, L. Liu, J. Power Sources 248 (2014) 91–100, http://dx.doi.org/10.1016/j.jpowsour.2013.09.052, URL: https://www.sciencedirect.com/science/article/pii/S0378775313015486.

[14] M. Casas-Cabanas, A. Ponrouch, M.R. Palacín, Isr. J. Chem. 61 (1–2) (2021) 26–37, http://dx.doi.org/10.1002/ijch.202000099.

[15] Z. Mao, M. Farkhondeh, M. Pritzker, M. Fowler, Z. Chen, Electrochim. Acta 222 (2016) 1741–1750, http://dx.doi.org/10.1016/j.electacta.2016.11.169.

[16] A. Klein, P. Axmann, M. Wohlfahrt-Mehrens, J. Electrochem. Soc. 163 (9) (2016) A1936–A1940, http://dx.doi.org/10.1149/2.0741609jes.

[17] C. Heubner, T. Liebmann, C. Lämmel, M. Schneider, A. Michaelis, J. Power Sources 363 (2017) 311–316, http://dx.doi.org/10.1016/j.jpowsour.2017.07.108.

[18] C. Heubner, T. Liebmann, C. Lämmel, M. Schneider, A. Michaelis, J. Energy Storage 20 (2018) 101–108, http://dx.doi.org/10.1016/j.est.2018.09.003.

[19] T. Liebmann, C. Heubner, C. Lämmel, M. Schneider, A. Michaelis, ChemElectroChem 6 (22) (2019) 5728–5734, http://dx.doi.org/10.1002/celc.201901554.

[20] T. Liebmann, C. Heubner, M. Schneider, A. Michaelis, Mater. Today Energy 22 (2021) 100845, http://dx.doi.org/10.1016/j.mtener.2021.100845.

[21] T. Kobayashi, Y. Kobayashi, H. Miyashiro, J. Mater. Chem. A 5 (18) (2017) 8653–8661, http://dx.doi.org/10.1039/C7TA02056B.

[22] D. Saurel, A. Pendashteh, M. Jáuregui, M. Reynaud, M. Fehse, M. Galceran, M. Casas-Cabanas, Chem. Methods 1 (6) (2021) 249–260, http://dx.doi.org/10.1002/cmtd.202100009, URL: https://chemistry-europe.onlinelibrary.wiley.com/doi/abs/10.1002/cmtd.202100009.

[23] M. Herklotz, J. Weiß, E. Ahrens, M. Yavuz, L. Mereacre, N. Kiziltas-Yavuz, C. Dräger, H. Ehrenberg, J. Eckert, F. Fauth, L. Giebeler, M. Knapp, J. Appl. Crystallogr. 49 (1) (2016) 340–345, http://dx.doi.org/10.1107/S1600576715022165.

[24] J. Rodríguez-Carvajal, Physica B 192 (1) (1993) 55–69, http://dx.doi.org/10.1016/0921-4526(93)90108-I, URL: https://www.sciencedirect.com/science/article/pii/092145269390108I.

[25] M. Fehse, A. Iadecola, M.T. Sougrati, P. Conti, M. Giorgetti, L. Stievano, Energy Storage Mater. 18 (2019) 328–337, http://dx.doi.org/10.1016/j.ensm.2019.02.002, URL: https://www.sciencedirect.com/science/article/pii/S2405829719300431.

[26] S. Jung, J. Power Sources 264 (2014) 184–194, http://dx.doi.org/10.1016/j.jpowsour.2014.04.072.

[27] R. Weber, C.R. Fell, J.R. Dahn, S. Hy, J. Electrochem. Soc. 164 (13) (2017) A2992, http://dx.doi.org/10.1149/2.0441713jes.

[28] T. Liu, L. Yu, J. Lu, T. Zhou, X. Huang, Z. Cai, A. Dai, J. Gim, Y. Ren, X. Xiao, M.V. Holt, Y.S. Chu, I. Arslan, J. Wen, K. Amine, Nature Commun. 12 (1) (2021) 6024, http://dx.doi.org/10.1038/s41467-021-26290-z, URL: https://www.nature.com/articles/s41467-021-26290-z, Number: 1 Publisher: Nature Publishing Group.

[29] T. Li, X.-Z. Yuan, L. Zhang, D. Song, K. Shi, C. Bock, Electrochem. Energy Rev. 3 (1) (2020-03-01) 43–80, http://dx.doi.org/10.1007/s41918-019-00053-3.

[30] K.R. Tallman, G.P. Wheeler, C.J. Kern, E. Stavitski, X. Tong, K.J. Takeuchi, A.C. Marschilok, D.C. Bock, E.S. Takeuchi, J. Phys. Chem. C 125 (1) (2021) 58–73, http://dx.doi.org/10.1021/acs.jpcc.0c08095, Publisher: American Chemical Society.

[31] Y.-N. Zhou, X. Yu, J. Liu, J. Bai, E. Dooryhee, Z.-W. Fu, E. Hu, H. Li, L.G. and* Kyung-Wan Nam, S.-M. Bak, X.-Q. Yang, Adv. Energy Mater. 6 (2016) 1600597, URL: https://onlinelibrary.wiley.com/doi/abs/10.1002/aenm.201600597.

[32] M. Fehse, N. Etxebarria, L. Otaegui, M. Cabello, S. Martín-Fuentes, M.A. Cabañero, I. Monterrubio, C.F. Elkjær, O. Fabelo, N.A. Enkubari, J.M. López del Amo, M. Casas-Cabanas, M. Reynaud, Chem. Mater. 34 (14) (2022) 6529–6540, http://dx.doi.org/10.1021/acs.chemmater.2c01360.

[33] H. Arai, K. Sato, Y. Orikasa, H. Murayama, I. Takahashi, Y. Koyama, Y. Uchimoto, Z. Ogumi, J. Mater. Chem. A 1 (2013) 10442–10449, http://dx.doi.org/10.1039/C3TA11637A.